

Stars as cosmic scales: measuring stellar mass with microlensed supernovae

Luke Weisenbach,^{1,*} Thomas Collett,¹ Wolfgang Enzi,¹ Lindsay Oldham,¹ Ana Sainz de Murieta¹

¹*Institute of Cosmology and Gravitation, University of Portsmouth, Burnaby Road, Portsmouth, PO1 3FX, UK*

Accepted XXX. Received YYY; in original form ZZZ

ABSTRACT

Gravitational microlensing is a unique probe of the stellar content in strong lens galaxies. Flux ratio anomalies from gravitationally lensed supernovae (gISNe), just like lensed quasars, can be used to constrain the stellar mass fractions at the image positions. Type Ia supernovae are of particular interest as knowledge of the intrinsic source brightness helps constrain the amount of (de)magnification from the macromodel predictions that might be due to microlensing. In addition, the presence or absence of caustic crossings in the light curves of gISNe can be used to constrain the mass of the microlenses. We find that a sample of 50 well-modeled gISNe Ia systems with single epoch observations at peak intrinsic supernova luminosity should be able to constrain a stellar mass-to-light ratio to within $\sim 15\%$. A set of systems with light curve level information providing the location (or absence) of caustic crossing events can also constrain the mass of the microlenses to within $\sim 50\%$. Much work is needed to make such a measurement in practice, but our results demonstrate the feasibility of microlensing to place constraints on astrophysical parameters related to the initial mass function of lensing galaxies without any prior assumptions on the stellar mass.

Key words: gravitational lensing: micro – gravitational lensing: strong – transients: supernovae

1 INTRODUCTION

Precisely how the matter content of galaxies is split between baryons and dark matter is a complex problem. Various methods for measuring the relative contributions of each have been explored, ranging from stellar population synthesis (SPS) (Conroy 2013), kinematics (Cappellari 2016), strong gravitational lensing (Shajib et al. 2024), and combinations thereof. In the case of the former, a fundamental input required for fitting the spectral energy distribution of a galaxy is the Initial Mass Function (IMF) of the stellar population. In tandem with the star formation rate, the IMF controls the Present Day Mass Function (PDMF) and therefore the present day total stellar mass. While there is increasing evidence for variations in the IMF among galaxies (Smith 2020), measurements of stellar mass across a variety of galactic parameters such as age, metallicity, and velocity dispersion may lend insight into the mechanisms by which the stellar populations of galaxies evolve.

In the case of gravitational lensing, the quantity that is best constrained by data is the total mass within the Einstein radius. Assuming functional forms for the dark and/or baryonic components and combining lensing with stellar kinematics can provide a measurement of the stellar mass (Treu & Koopmans 2004; Sonnenfeld et al. 2012, 2015) while breaking some degeneracies. Results for different samples of lenses favor either Chabrier (Sonnenfeld et al. 2019) or Salpeter IMFs (Spiniello et al. 2011, 2012; Shajib et al. 2021), though constraints depend on the functional forms used as well as how the

stellar mass is parametrized, with some tentative hints of trends with velocity dispersion (Treu et al. 2010).

In all cases, the (dis)agreement with specific IMFs relies on comparing the inferred stellar mass from lensing to that from SPS. Along with the shape and slope of the IMF, such results are sensitive to the low mass cutoff used in the IMF – which can significantly change the stellar mass-to-light ratio Y_\star (Barnabè et al. 2013; Conroy et al. 2017; Newman et al. 2017). While lensing is sensitive to the total two dimensional projected mass, a portion of that mass is due to stellar remnants, planets, and stars near the hydrogen burning limit which do not contribute significantly (if at all) to the measured light (Schechter 2018). They do, however, source small scale gravitational lensing deflections.

When a background source is appropriately aligned behind a foreground galaxy, the gravitational potential of the galaxy distorts and (de)magnifies the image of the source, at times creating multiple images if the alignment is fortuitous. The stars within the lensing galaxy also act as lenses in their own right (Chang & Refsdal 1979; Young 1981; Paczynski 1986), further perturbing the multiple images when the source is of a sufficiently small size. Known as microlensing, this effect is sensitive to all compact objects in the lens galaxy along the line of sight. This makes it a unique probe of the stellar mass fraction, and therefore the PDMF, that does not depend on assumptions about the stellar mass-to-light ratio or the stellar mass profile – just the total mass profile, which is typically well constrained by the separations between macroimages.

For the majority of strong lensing history, the only sources of sufficient compactness to allow for such microlensing to occur have been

* E-mail: weislake@alum.mit.edu

quasars (Walsh et al. 1979; Irwin et al. 1989; Schmidt & Wambsgans 2010). However, recent discoveries of gravitationally lensed supernovae (gISNe) (Goobar et al. 2017, 2023) have opened a new door for microlensing studies. Microlensing is as ubiquitous for lensed supernovae (Dobler & Keeton 2006; Suyu et al. 2024) as it is for lensed quasars (Witt et al. 1995; Vernardos et al. 2024), and given the wealth of gISNe expected to be discovered by the Vera Rubin Observatory (LSST) in the next decade (Goldstein et al. 2019; Wojtak et al. 2019; Sainz de Murieta et al. 2023; Arendse et al. 2024) it is worth understanding precisely what information can be gleaned from them.

Much work has already been done on the utility of gISNe, specifically Type Ia supernovae (gISNe Ia), as probes of cosmology through time delay cosmography (Goldstein et al. 2018; Foxley-Marrable et al. 2018; Huber et al. 2019; Pierel & Rodney 2019; Huber et al. 2021). Other works have examined how gISNe can be used to constrain the total mass profile of the lens galaxy (Mörtzell et al. 2020; Diego et al. 2022); gISNe Ia shine here as their ‘standardizable candle’ nature might permit breaking the mass-sheet degeneracy (Falco et al. 1985; Schneider & Sluse 2014) and testing lens modeling systematics – though only if microlensing is negligible compared to the intrinsic scatter in the luminosity of the Ia population (Foxley-Marrable et al. 2018; Weisenbach et al. 2024). In the cases where microlensing is not negligible however, the problem can be flipped around: rather than using gISNe Ia to probe cosmology, reasonable assumptions on cosmological parameters instead turn them into probes of the stellar content of the lensing galaxy.

Various microlensing constraints on the IMF have been made using lensed quasars in both the X-ray and optical (see Vernardos et al. 2024 for a review). Constraints are typically on either some constant stellar mass fraction (Pooley et al. 2009; Mediavilla et al. 2009) or a constant stellar mass-to-light ratio (Schechter et al. 2014). In the case of the former, the assumption of constancy seems roughly appropriate if the images are all at similar distances from the center of the lens. The latter approach may be more robust, though mass-to-light gradients in the lens galaxy could alter results. More generally however, what microlensing allows us to *actually* measure is the stellar mass-to-light ratio of the PDMF at the image positions. Precisely how such measurements then relate to constraints on the IMF depends on assumptions one may or may not wish to make or test.

In addition to constraining the stellar mass fraction, microlensing also probes the typical mass of a compact object at the image locations. Sensitivity to mass at the lower end of the mass spectrum is important for constraining the low mass cutoff of the IMF, which along with the shape of the mass spectrum determines the mean mass (see the range in, e.g., Table 2 of Parravano et al. 2011, for various IMFs). The finite size of the source is an extremely important nuisance factor in such measurements (Lewis & Gil-Merino 2006), but joint constraints of quasar source size and typical stellar mass have been made (Mediavilla et al. 2017; Jiménez-Vicente & Mediavilla 2019).

Supernovae offer a host of improvements over quasars that are beneficial. They 1) evolve over shorter timescales, requiring less observational investment in light curve monitoring; 2) fade away, permitting better followup of the lens and host galaxy light for modeling; and 3) have better understood sizes, luminosities, and light curve evolution (Phillips 1993; Kenworthy et al. 2021), which allows for easier microlensing analyses. Dobler & Keeton (2006) noted that “...the amount of structure in the [microlensed] light curves is a sign that more effort should be exerted to figure out how to analyze lensed SN light curves to determine properties of the stellar population.” The purpose of this work is to exert just such an effort on constrain-

ing 1) the fraction of matter in the form of compact objects and 2) the typical mass of those compact objects, at the positions of lensed supernovae images.

In Section 2, we review how microlensing can be used to constrain the stellar mass fraction and the typical mass of compact objects. In Section 3, we discuss the mock data used in this work. In Section 4, we explore how well we can recover the stellar mass fractions from a population of gISNe Ia. In Section 5, we further examine how well we can jointly constrain the stellar mass fraction and the microlens mass. We discuss some limitations of our work in Section 6, and present conclusions and discussions in Section 7.

2 MICROLENSING CONSTRAINTS ON STELLAR MASS PARAMETERS

In this section, we provide an overview of why microlensing can be used to constrain the typical mass of compact objects and the stellar mass fraction in the lens galaxy.

2.1 Constraining the microlens mass

It is well known that the physical size of the source, relative to the characteristic length scale (Einstein radius) of the microlenses, is one of the main factors that drives microlensing variability – more so than the projected two dimensional luminosity profile of the source (Mortonson et al. 2005; Vernardos & Tsagkatakis 2019). Since supernovae expand at rates of tens to a few tens of thousands of km/s (Takáts & Vinkó 2012; Zheng et al. 2018), we might therefore expect to learn most easily about the average mass of the microlenses. The situation is somewhat complicated by the fact that a spectrum of masses from a PDMF introduces a range of length scales which may be relevant for microlensing at different points in time. We limit ourselves in this work to the simplest scenario where all the microlenses have the same mass, though we discuss the implications of a mass spectrum in Section 6. We fully explore how well this single mass can be constrained with fairly simple considerations in Section 5, but we provide some motivation for such constraints below.

Unlike quasars which have a fixed size and move through the microcaustic network, supernovae have a fixed position and expand in size through the microcaustic network. This allows us to measure the microlens mass from the time (or lack of time) at which the first caustic crossing event occurs in the light curve, so long as we know the expansion velocity of the supernova. Using the locations of the microcaustics, we can determine the distance to the nearest caustic d_{caustic} as a function of source position (shown in Figure 1) in units of the Einstein radius of the microlenses θ_{\star} , which scales with the mass m_{\star} of the microlenses as $\theta_{\star} \propto \sqrt{m_{\star}}$. A large microlens mass means an increased separation (in physical units) between caustics, decreasing the likelihood a caustic crossing should occur as the supernova expands. Conversely, a small microlens mass means a decreased separation between caustics and an increased chance of a caustic crossing.

To highlight this, we create 50 realizations of microlensing light curves for a single macroimage using the procedures outlined later in Section 3. For an individual light curve, the probability of mass m_{\star} given the caustic crossing time t_{caustic} is

$$p(m_{\star}|t_{\text{caustic}}) \propto p(t_{\text{caustic}}|m_{\star})p(m_{\star}) \quad (1)$$

We take $p(m_{\star})$ to be a uniform prior between 0.01 and $2 M_{\odot}$. The likelihood $p(t_{\text{caustic}}|m_{\star})$ is related to $p(d_{\text{caustic}}|\theta_{\star})$, assuming a known expansion velocity. We can therefore directly translate the

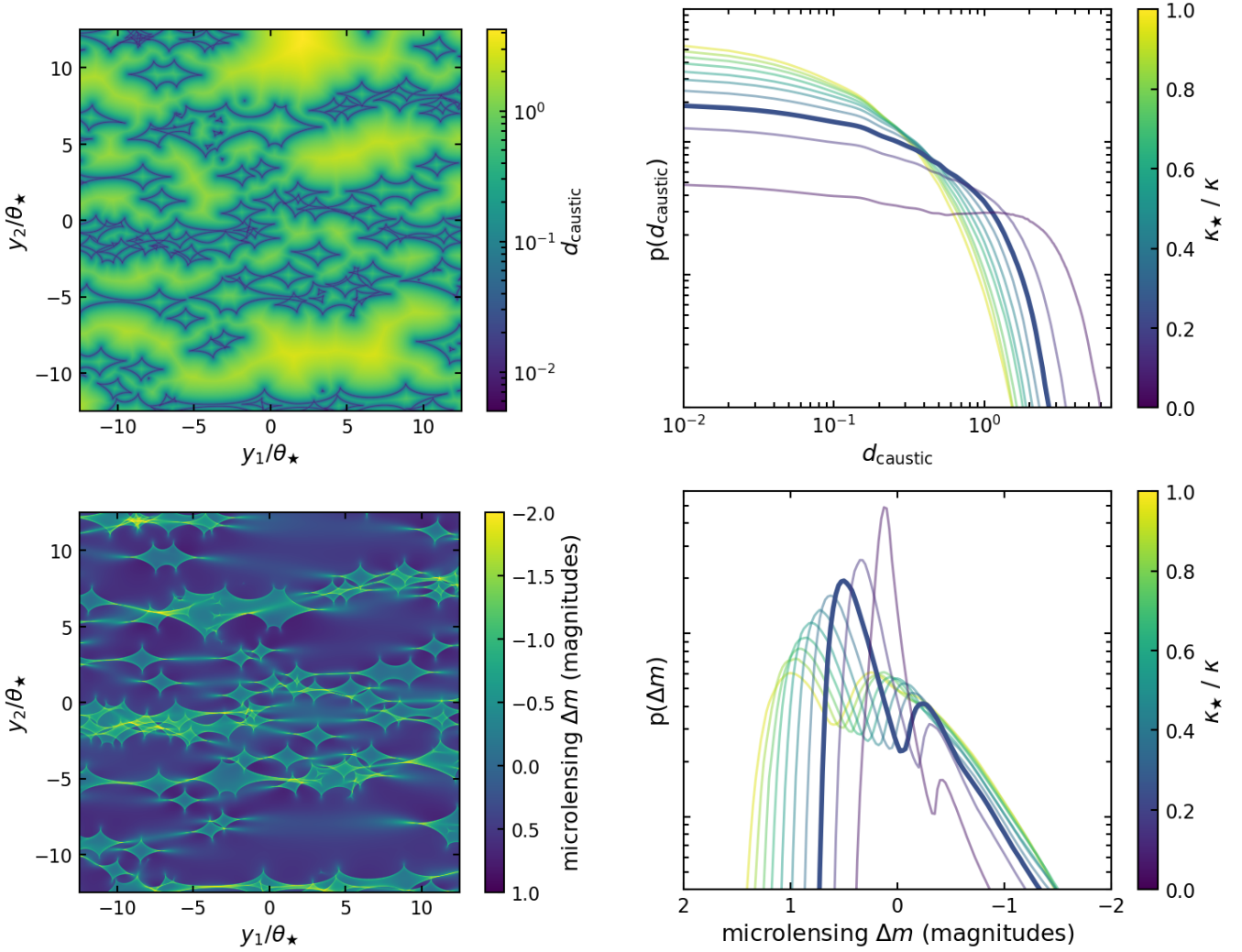


Figure 1. Visualization of the distance to the nearest caustic d_{caustic} (top left) and the microlensing (de)magnification Δm relative to the macromodel (bottom left) as a function of position in the source plane for $\kappa = \gamma = 0.4$. The probability distributions of d_{caustic} and Δm are shown in the right column. The thick lines show the specific distributions for the value of κ_{\star}/κ of the left column, while the thinner opaque lines show how the distributions change with and are highly sensitive to the ratio κ_{\star}/κ . We show examples of the joint distributions of d_{caustic} and Δm in Figure 4 which highlight the strong correlations between the variables.

distribution of distance-to-caustics into a posterior on the mass given some observed time (or absence) of caustic crossing.

Posteriors for the 50 light curves are shown in Figure 2. As expected, light curves which have caustic crossings at early times heavily favor low mass microlenses. As the time of caustic crossing increases, the probability of low mass decreases, while the probability of high mass increases. If no caustic crossing is seen within the time of observations, the posterior for the mass uses the integrated probability from the maximum observation time to the maximum distance to a caustic. While an individual light curve does not have much useful constraining power, the final combination of 50 light curves does – with a peak at $m_{\star} \approx 0.38M_{\odot}$, though the distribution is skewed with $m_{\star} = 0.54^{+0.44}_{-0.23}M_{\odot}$ (68% confidence interval). The posterior has scattered high from truth ($m_{\star} = 0.3M_{\odot}$) in this example due to Poisson noise in the number of the 50 curves that crossed a caustic.

2.2 Constraining the stellar mass fraction

While light curves provide ample information about the fraction of matter in the form of compact objects, one can also glean such constraints from single epoch flux ratio anomaly measurements (Schechter & Wambsganss 2002); each of the methods have their merits and drawbacks (see Vernardos et al. 2024 for a review). The idea behind measuring the stellar mass fraction from microlensing uses the fact that the distribution of microlensing magnification is highly sensitive to the value of the stellar mass fraction at the image locations, as shown in the bottom right of Figure 1. Some values of (de)magnification strongly favor particular stellar mass fractions, and can even rule out some values of κ_{\star} . In general, one can use the flux ratios between pairs of images to calculate the likelihood of κ_{\star} for each image based on the observed magnification ratios and the microlensing magnification distributions.

Supernovae provide an additional boon over lensed quasars in that the size of the source is better constrained. The X-ray emitting re-

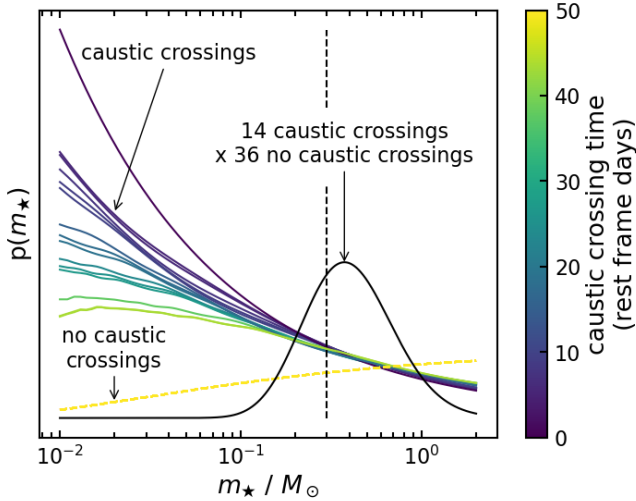


Figure 2. Posteriors (colored curves) of m_* for 50 different microlensing light curves from the same macroimage, and their product (black curve). The vertical dashed black line denotes the true value ($m_* = 0.3M_\odot$) used when creating the mock data. Light curves which do not cross caustics all have the same dashed yellow posterior. Posteriors from individual light curves do not well constrain the mass, but highlight the dependence on the caustic crossing time.

gions of quasars are the most ideal for microlensing measurements as they come from a compact region which can generally be considered as point-like, or at least much smaller than the region which emits in the visible or larger wavelengths (Pooley et al. 2006, 2007). Supernovae also start off orders of magnitude smaller than the Einstein radii of the microlenses; for representative source and lens redshifts of 0.4 and 0.8 (respectively) with microlenses of mass $0.3M_\odot$, a supernova expanding at 10^4 km/s reaches a size of $\sim 0.2\theta_*$ after 50 rest-frame days. Treating supernovae as point-like is an acceptable approximation for some microlensing purposes (compare Foxley-Marrable et al. 2018 and Weisenbach et al. 2021), easing the need to jointly model the size and profile of the source. Should one wish to be more precise, the expansion speed of supernovae can be determined from spectral lines (Kirshner & Kwan 1974; Eastman et al. 1996; Dessart & Hillier 2005; Takáts & Vinkó 2012), providing a prior on the source size that can be used when modeling. Theoretical supernovae explosion models can also provide half-light radii as a function of wavelength and time (Goldstein et al. 2018; Huber et al. 2019), which will likely permit multispectral observations and modeling to provide more stringent constraints than this work in the future.

Furthermore, Type Ia supernovae constrain an additional unknown – the intrinsic brightness of the source. Having an informed prior on the source brightness constrains the microlensing (de)magnification¹ and is important for reducing the number of gravitationally microlensed systems required to make interesting conclusions.

3 MOCK DATA

We use a set of simulated gISNe Ia from Sainz de Murieta et al. (2023) as our mock data set, with a cut on image separation $> 0.8''$ (i.e. resolvable). We also restrict ourselves to source redshifts for

¹ if we ignore millilensing

which the supernovae would be observable at peak in the absence of lensing, to guarantee that at least one image is observed². The catalog contains the macromodel parameters for simulated lenses and the positions and convergence values for the images of the sources. We model the stellar mass at the image locations with an elliptical de Vaucouleurs profile for the light aligned with the SIE potential of the lens (Vernardos 2019). Effective radii for the lenses are calculated from their velocity dispersions using the scaling relations in Hyde & Bernardi (2009). We then determine the mock stellar mass fractions assuming a Chabrier IMF, using fits for the dark matter fraction within half the effective radius from Auger et al. (2010).

We simulate microlensing magnification maps for the image parameters, using a mass of $m_* = 0.3M_\odot$ for all the microlenses. A true microlensed magnification light curve is generated for each image assuming a uniform disk for the supernova profile that is expanding at 10^4 km/s in the network of microcaustics. We take the light curves to extend up to 50 days in the rest frame. We simulate the lensed magnitude in the *i* band using the microlensed magnification and the spectroscopic templates of Hsiao et al. (2007) for the unlensed brightness, adding a 0.1 mag Gaussian scatter to mimic the intrinsic scatter present in the brightness of the Ia population after standardization. We add a further 0.01 mag uncertainty on the magnification to simulate observational photometric uncertainties.

In Section 4, we use the brightness of the lensed images at peak intrinsic luminosity. Essentially, this assumes that we discover the gISNe before the first image reaches peak, and have observations at peak for both images. In Section 5, we will use some information from the light curves, which again assumes discovery of the first image before it reaches peak intrinsic luminosity, along with adequate monitoring of it and subsequent images as the light curve evolves.

We note that while the catalog contains all images, the number of observed images for a double can be 1 if the second (saddlepoint) image is too demagnified to be observed. Similarly, a quad may have less than 4 detected images. We use sample sizes of 50 or 200 systems in the following sections; there was one quad in the sample of 50, and 3 in the sample of 200. While doubles in general do not outnumber quads by the ratio suggested here (Sainz de Murieta et al. 2023), our requirement that the images be well separated reduces the number of quads in the catalog that are usable for our purposes. Quadruply imaged gISNe Ia from small Einstein radii systems such as the two currently known galaxy-scale cases (Goobar et al. 2017, 2023) have more stringent observation requirements such as adaptive optics or space based followup, but pose an excellent way to probe the stellar content in small mass galaxies (Mörtzell et al. 2020; Arendse et al. 2025).

4 CONSTRAINING THE STELLAR MASS FRACTION

In this section, we discuss the methodology for constraining the stellar mass fraction at the image locations, with results for how well we can recover the input values from our simulations.

4.1 Methodology

We assume that, for each system, we can perfectly measure the convergence κ at the image locations as well as the effective radius and ellipticity of the lens. Our goal then is to determine how well we can recover the stellar mass fractions based on the microlensing

² This requires a peak brightness ≥ 24 mag for LSST.

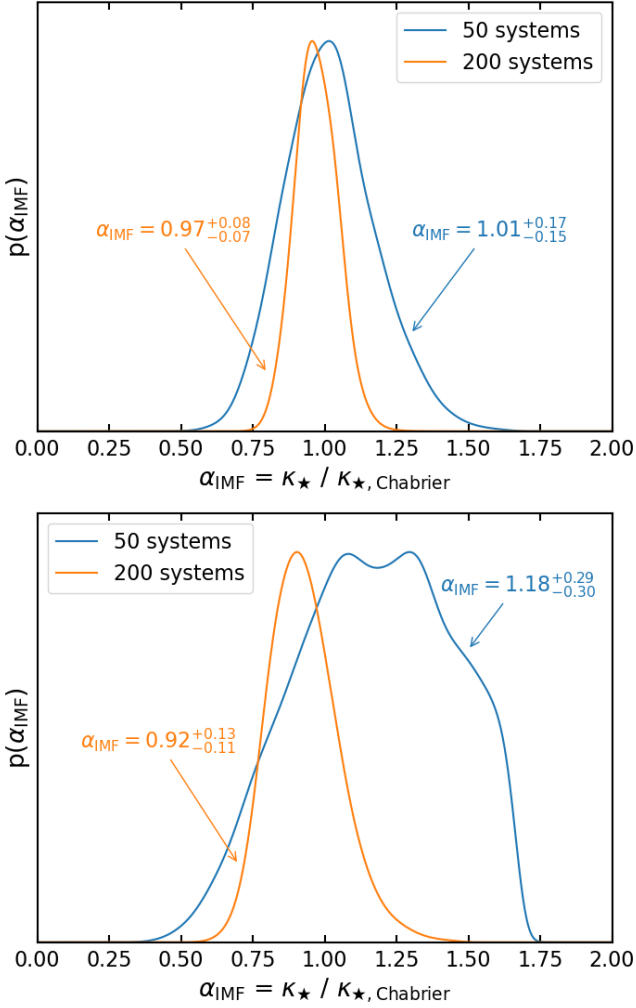


Figure 3. Posteriors of α_{IMF} for 50 or 200 gISNe Ia systems, assuming an uncertainty for the intrinsic source brightness of 0.1 mag (top) or 0.3 mag (bottom). The true value is $\alpha_{\text{IMF}} = 1$. In the case of larger uncertainty for the intrinsic source brightness, the sharp cutoff near $\alpha_{\text{IMF}} \approx 1.75$ is because κ_{\star} must be $\leq \kappa$.

(de)magnifications. While microlensing measures κ_{\star} , the underlying physical phenomenon which drives the value of κ_{\star} is the stellar mass-to-light ratio Y_{\star} . Following Schechter et al. (2014), we take the free parameter of the problem to be the ratio of the value of κ_{\star} measured from microlensing to a fiducial $\kappa_{\star, \text{IMF}}$ calculated from a specific IMF, i.e. an IMF mismatch α_{IMF} (Treu et al. 2010) (which is equivalent to letting the free parameter be Y_{\star}). We use Chabrier as our fiducial IMF as well, and denote the free parameter as

$$\alpha_{\text{IMF}} = \frac{\kappa_{\star}}{\kappa_{\star, \text{Chabrier}}} \quad (2)$$

This means that we expect to recover a value of $\alpha_{\text{IMF}} = 1$, and the goal is to see just how well we are able to do so with varying sample sizes and uncertainties.

For the macromodel convergence κ and shear γ of each image, we create microlensing magnification maps using inverse polygon mapping (Mediavilla et al. 2006, 2011) combined with the fast multiple method (Greengard & Rokhlin 1987) for approximating the deflection angle of distant microlenses (Jiménez-Vicente & Mediavilla 2022), implemented on a GPU to speed up calculations by

orders of magnitude (Weisenbach et al., *in prep.*) and make the analyses tractable. We sample the smooth matter fraction $s = 1 - \frac{\kappa_{\star}}{\kappa}$ in discrete steps of $\Delta s = 0.02$ and average multiple maps for each (κ, κ_{\star}) pair to reduce noise in the final microlensing magnification distributions.

For each system, we are in general interested in the posterior

$$p(\alpha_{\text{IMF}}, m_s, m_j, R_{1/2}, m_{\star} | D) \quad (3)$$

of α_{IMF} , the true unlensed source brightness (in magnitudes) at peak intrinsic luminosity m_s , the true microlensed image brightnesses (in magnitudes) m_j (where the index j runs over the number of images), the half-light radius of the supernova $R_{1/2}$, and the microlens mass m_{\star} , given some data D which consists of the observed brightnesses of the images in the i band. For this section, we eventually want to marginalize over all other parameters to get $p(\alpha_{\text{IMF}} | D)$. The posterior is equal to

$$p(\alpha_{\text{IMF}}, m_s, m_j, R_{1/2}, m_{\star} | D) = p(D | \alpha_{\text{IMF}}, m_s, m_j, R_{1/2}, m_{\star}) \times p(\alpha_{\text{IMF}}, m_{\star}) p(m_s) p(m_j) p(R_{1/2}) \quad (4)$$

where the likelihood $p(D | \alpha_{\text{IMF}}, m_s, m_i, R_{1/2}, m_{\star})$ is taken to be the product of the microlensing magnification probability for the individual images (as they are all independent).

The prior for m_s is a Gaussian centered on the Hsiao et al. (2007) template magnitude for the source redshift; we will explore the effects of various levels of uncertainties in the source brightness. The priors on m_j are Gaussians centered on the observed values with widths equal to the observational uncertainties. The prior on $R_{1/2}$ should in general come from measurements of the expansion velocity using spectra; in this work we will assume the size is known exactly. The prior for $p(\alpha_{\text{IMF}}, m_{\star})$ might come from SPS models; as we are interested in how well microlensing can constrain the parameters with no other information, we take a uniform prior subject only to the constraint that κ_{\star} is positive and can never be greater than the total convergence³.

We make two simplifying assumptions to reduce the dimensionality of the parameter space. First, while our mock data were created using expanding supernova profiles, we model them here as point sources to avoid the computational burden of convolving magnification maps. This removes $R_{1/2}$ and any sensitivity to m_{\star} ; we will return to this approximation in Section 5. Second, we choose to ignore the small observational errors in the image magnitudes, as they are expected to be of order 0.01 mag for LSST – an order of magnitude smaller than the scatter in the intrinsic brightness of the Ia population. This essentially removes m_j , absorbing the observational uncertainties into the intrinsic luminosity error.

We can therefore directly evaluate the simpler posterior

$$p(\alpha_{\text{IMF}} | D) = \int p(D | \alpha_{\text{IMF}}, m_s) p(m_s) dm_s \quad (5)$$

for each system. The product of $p(\alpha_{\text{IMF}} | D)$ for all systems then gives us our final constraint on α_{IMF} .

We note that we are limited by microlensing simulations to sampling the parameter space in discrete values of Δs . These do not necessarily correspond to the same discrete values of α_{IMF} for each

³ In practice, the likelihood is actually calculated in terms of κ_{\star} and then converted to a posterior on α_{IMF} . The tophat prior that ensures κ_{\star}/κ lies between 0 and 1 corresponds to tophat prior between 0 and a different maximum α_{IMF} for each image.

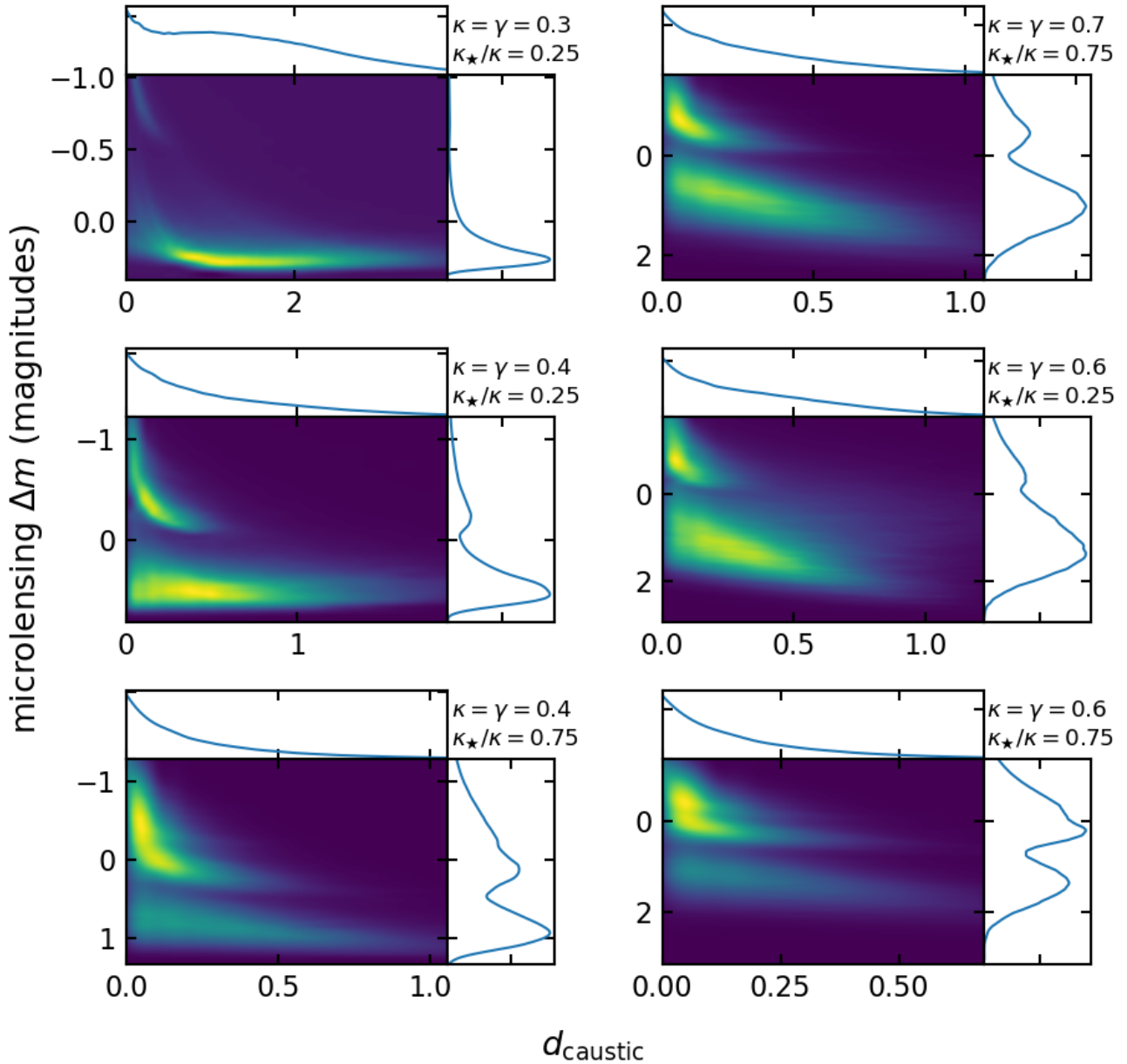


Figure 4. Joint probability distribution of the magnification and the distance to the nearest caustic for various $\kappa = \gamma$ and κ_\star values. Distances are in units of the Einstein radius of the microlenses θ_\star . Note the different axes scales for each subplot, particularly for d_{caustic} .

image within a system⁴, which almost certainly introduces some amount of systematics into the results. We interpolate the system posteriors using kernel density estimators before multiplying them to get the final posterior on α_{IMF} .

4.2 Results

We initially test how well we recover α_{IMF} with 50 simulated gISNe Ia systems, which is roughly the number estimated to be found in $\sim 2-3$ years of LSST observations (Sainz de Murieta et al. 2023; Arendse et al. 2024). This is also a realistic number to be observationally

followed up in ~ 5 years for H_0 studies; our measurements are unlikely to require any extra resources on top of what is needed for time delay cosmography. We also examine how results improve with a larger number (200) of gISNe Ia. Figure 3 shows our results when the error on the intrinsic source brightness is taken to be 0.1 or 0.3 mag. In the case of 50 systems and a 0.1 mag error on the intrinsic source brightness, α_{IMF} is recovered to within $\sim 15\%$; in all cases, the true value of $\alpha_{\text{IMF}} = 1$ is recovered within the one sigma bounds. We note once more that the prior on α_{IMF} is uniform between 0 and a physical upper bound that κ_\star can never exceed κ .

Since lenses are typically passive elliptical galaxies, a Salpeter IMF would have a value of $\alpha_{\text{IMF}} \approx 1.6-1.7$ (depending on age and metallicity, Cappellari et al. 2012; Bernardi et al. 2018), which means that 50 gISNe Ia should be able to discriminate between a Salpeter and Chabrier IMF at the $\sim 4\sigma$ level if the error on the

⁴ Especially for the saddlepoint images where κ is larger and a small step in Δs is a larger step in α_{IMF} than for the images which are minima.

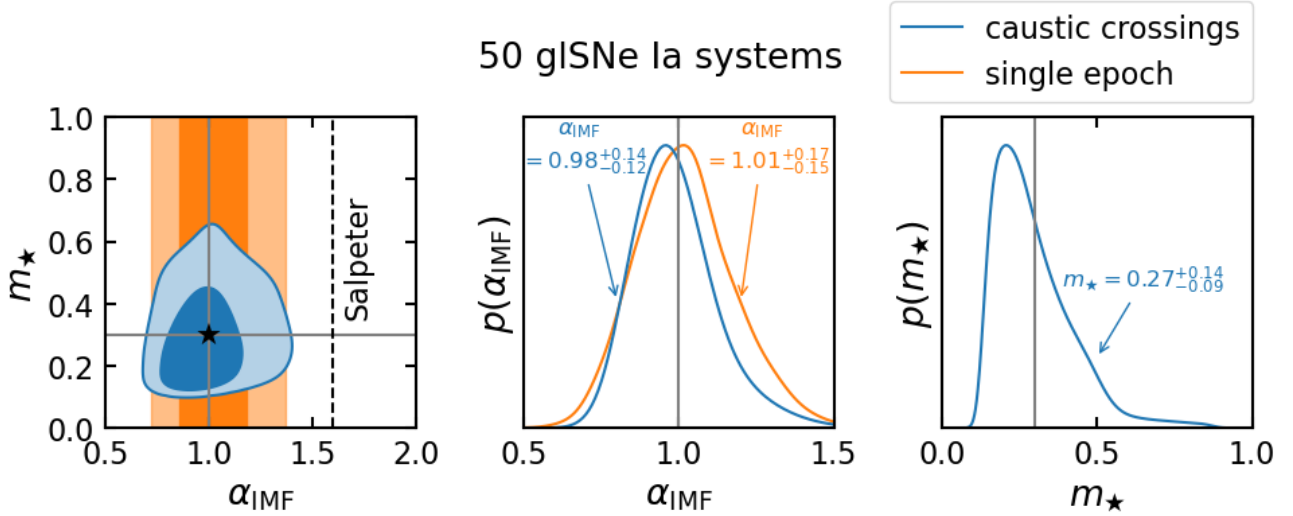


Figure 5. Joint posterior of α_{IMF} and m_{\star} for 50 gISNe Ia systems, assuming a 0.1 mag error on the intrinsic source brightness, a uniform prior on α_{IMF} such that $\kappa_{\star} \leq \kappa$, and a uniform prior between 0 and $1 M_{\odot}$ for m_{\star} . Solid and opaque contours denote the 68% and 95% confidence intervals respectively. The black dashed line marks the approximate value of α_{IMF} for a Salpeter IMF. We include the constraints from Figure 3 (single epoch) for comparison. See Figure A1 for constraints with more systems and different errors on the source brightness.

intrinsic source brightness is 0.1 mag. Increasing the uncertainty on the source brightness to 0.3 mag requires ~ 200 systems to make similar constraints. Since α_{IMF} is equivalent to Y_{\star} , this means that a population of gISNe Ia should be able to constrain Y_{\star} to $\sim 15\%$. Some additional, but likely subdominant, errors will also come from propagating measurements of the lens light and total lens galaxy mass.

5 CONSTRAINING THE MEAN MICROLENS MASS

In addition to constraining the stellar mass fraction at the image locations, light curve level data are sensitive to the mean mass of the microlenses. Some microlensed light curves will experience caustic crossing events which cause drastic changes in magnification. Due to the scaling of the Einstein radius of the microlenses with their mass, the presence or absence of caustic crossings informs us about the length scale involved so long as we know about the relative size of the supernovae. One can get the expansion velocity from spectral lines, providing a prior on the source size (Kirshner & Kwan 1974; Eastman et al. 1996; Dessart & Hillier 2005; Takáts & Vinkó 2012). For simplicity, we assume that we know the supernova size perfectly and that the time of caustic crossing is known to within a day from the observed light curves. We are then interested in adding one additional parameter back to the problem, the microlens mass m_{\star} .

5.1 Likelihood simulations

We use a GPU implementation of Witt’s (1990) method to calculate the critical curves of the microlenses (Weisenbach, *in prep.*), from which we can locate the caustics and create a map of the number of microminima (Wambsganss et al. 1992; Granot et al. 2003), or equivalently the number of caustic crossings (NCC). While convolving the magnification map with the uniform disk profile of the source gives a light curve, convolving the NCC map with circular min/max filters of the same size gives two curves which together provide the

location of the first caustic crossing (or whether no caustic crossing is present).

From the NCC map we can also determine, for any pixel, the distance to the nearest caustic using a Euclidean distance transform (Fabbri et al. 2008), shown in Figure 1 (top left). Combining the magnification and NCC maps, we have a two dimensional distribution of magnification and distance to nearest caustic (Figure 4), which becomes the likelihood for the joint probability of α_{IMF} and m_{\star} .

5.2 Joint constraints

We jointly constrain α_{IMF} and m_{\star} using both the observed magnification and the presence (or absence) of caustic crossings. This is similar to quasar studies which have jointly constrained the size of the quasar accretion disk and the microlens mass (Mediavilla et al. 2017; Jiménez-Vicente & Mediavilla 2019). The Bayesian framework is that discussed in Section 4, but we add back in the microlens mass m_{\star} as a parameter and the time of caustic crossing as additional data, and use the joint probability distribution of the microlensing magnification and the distance to the nearest caustic as our likelihood.

We show in Figure 5 the constraints for 50 systems, assuming a 0.1 mag uncertainty on the intrinsic source brightness and a uniform prior on m_{\star} between 0 and $1 M_{\odot}$. As before, α_{IMF} is constrained to within $\sim 15\%$. The constraints on m_{\star} are more broad, but the input of $0.3 M_{\odot}$ is well recovered.

If the number of supernovae systems is increased from 50 to 200 while maintaining a 0.1 mag uncertainty on the source brightness, the constraints on α_{IMF} improve from $0.98^{+0.14}_{-0.12}$ to $1.01^{+0.07}_{-0.06}$, while the constraints on m_{\star} improve from $0.27^{+0.14}_{-0.09}$ to $0.27^{+0.07}_{-0.06}$. Increasing the source brightness uncertainty to 0.3 mag while maintaining 200 systems changes the constraints to $\alpha_{\text{IMF}} = 1.12^{+0.11}_{-0.10}$ and $m_{\star} = 0.27^{+0.10}_{-0.06}$ (see also Figure A1). In general, the constraints on α_{IMF} appear more sensitive to changes in source brightness uncertainties than the constraints on m_{\star} .

6 CAVEATS

We assume that the macro-model for the lens is known precisely. This will, in general, not be true. In particular, the mass-sheet degeneracy (Falco et al. 1985; Schneider & Sluse 2014) introduces uncertainties into the convergence which are important for microlensing, as κ is a necessary constraint for microlensing measurements. However, either the Hubble constant and measurements of the time delays between images or lens velocity dispersions can be used to constrain the macro-model. In practice therefore, a true analysis would require marginalizing over values of κ and γ in the lens macro-model, which may significantly affect the microlensing likelihoods in some regions of parameter space (Vernardos & Fluke 2014). This would require image level data and lens modeling which, while outside the scope of this work, will be important to implement for future gISNe discoveries.

As previously mentioned, the majority of systems in the catalog of mocks used here are doubly imaged supernovae. The lens models for such systems are typically under-constrained if only the images of the supernovae are seen. Having a lensed host galaxy makes the modeling easier, but only $\sim 50\%$ of gISNe will have a lensed host with a smaller ($\sim 25\%$) fraction having a lensed host which is bright enough to observe (Sainz de Murieta et al. 2024). Quadruply lensed systems have better macromodel constraints on κ and γ , and close pairs of fold images are ideal for constraining Y_\star (Schechter & Wambsganss 2002), but they consist of a smaller population. The case of a 0.3 mag uncertainty on the intrinsic source brightness can be considered as an imperfect proxy for inflating the errors from uncertain lens models, highlighting the larger number of systems that might be required for precise constraints.

While we ignore the size of the source, a better analysis would consider the joint likelihood of microlensing magnification, d_{caustic} , and source size. However, the magnification of a supernova that does not cross a microcaustic is essentially constant over its lifetime, changing nothing in our results. A supernova that does cross a microcaustic will experience a change in magnification which may help constrain α_{IMF} and m_\star better, but the limited number of such supernovae and the fact that our posteriors still capture the true values suggests that d_{caustic} provides enough information and further improvements would be minimal.

Our analyses lack in one area which will be important to explore in the future. While a given IMF determines the stellar mass fraction at the image positions, it also determines the PDMF. The dependence of microlensing on the mass spectrum is usually ignored, largely due to the fact that it is difficult to manifest in magnification distributions. It was originally conjectured to bear little to no role (Wambsganss 1992; Lewis & Irwin 1995, 1996), though that was later disproven by Schechter et al. (2004). The dependence is minimal in microlensed quasars for physical reasons (Lewis & Gil-Merino 2006) which are also relevant for supernovae: at a fixed size the source is blind to masses below some cutoff. Microlensing studies must therefore be careful to state the mass range for which results about the typical mass are valid when incorporating constraints on the source size.

Convolutions of the microlensing magnification maps with a source profile wash out the contributions of low mass microlenses, making them act as a smooth component indistinguishable from dark matter. Although we use a single mass for all of the microlenses for our simulations and subsequent constraints, a proper analysis of real data would need to consider a spectrum of masses given by the PDMF. This widens the parameter space, as one must then worry about the upper and lower mass cutoffs as well as the slope (and other possible parameters governing the shape) of the mass spectrum. While such

simulations are feasible with current computational resources for microlensing, they do multiply the necessary time – which already took \sim weeks to generate the necessary microlensing likelihoods for our efforts. The development of (semi)analytic expressions or approximations for the microlensing likelihoods are desirable and would make future analyses more tractable.

7 DISCUSSION AND CONCLUSIONS

The present day stellar mass in galaxies is dependent on both the initial stellar population and subsequent star formation history. Estimates of stellar mass from SPS can be uncertain by factors of ~ 2 or more, depending on stellar evolution uncertainties, initial galactic metallicity distributions, and assumptions regarding the IMF (Conroy et al. 2009). Robust independent measurements of stellar mass provide a means for testing SPS models and probing IMF dependencies on galactic parameters such as metallicity, velocity dispersion, and redshift. Contrary to methods which infer stellar mass from measured light, gravitational microlensing provides a unique way to directly probe the mass of compact objects in lensing galaxies using their gravitational effect. Microlensing can simultaneously measure the fraction of mass in compact objects and the mean mass of those objects, directly providing constraints on the lens galaxy PDMF and hence indirectly on the IMF.

In this work, we have used a simulated sample of gISNe Ia to examine how well we can jointly constrain an IMF mismatch parameter α_{IMF} (equivalent to a stellar mass-to-light ratio Y_\star) and the mean stellar mass m_\star of the microlenses, by exploiting observed magnifications of gISNe Ia and the timings of caustic crossings as the SN expands. With a sample of 50 gISNe Ia systems, we consistently recover our input α_{IMF} and m_\star values within the 68% confidence intervals of the posteriors. The value of α_{IMF} is recovered to within $\sim 15\%$ if the uncertainty on the intrinsic brightness of the source is 0.1 mag, while m_\star is constrained to within $\sim 50\%$. While we used total stellar mass estimates in our simulations from strong lensing fits (Auger et al. 2010) with a Chabrier IMF, a Salpeter IMF would differ by a factor of ~ 1.6 (van Dokkum et al. 2017; van Dokkum & Conroy 2024), making our microlensing constraints a $\sim 4\sigma$ discriminator between the two.

The mean stellar mass is not constrained enough to differentiate between IMFs, even when the number of systems is increased to 200. If the first image is discovered early enough, gravitational lensing allows us to predict when and where the second image will appear (Foxley-Marrable et al. 2020). Early observations of gISNe (when the SN photosphere is physically small) should be sensitive to the low mass end of the PDMF. While our work has assumed a single mass microlens population, our approach should generalize to a mass spectrum and there is hope for better constraints if some of our simplifying assumptions are removed; Wyithe & Turner (2001) showed that lightcurve variability statistics for lensed quasars can be inverted to obtain the microlens mass spectrum, a promising result which should also be explored for gISNe.

While the exact precision of our results should be viewed cautiously given the simplifications we made regarding lens modeling, our results suggest that even with minimal priors gISNe Ia have excellent sensitivity with which to probe the stellar mass content of lens galaxies and constrain their average IMF. Even if we have underestimated errors by a factor of 2, microlensing of 50 gISNe Ia would still be a 2σ discriminator between a Chabrier and Salpeter-like IMF in lens galaxies.

Multispectral observations of gISNe should provide slightly im-

proved constraints from what we expect, as the measurement of κ_* does not greatly depend on the filter used since the supernova size does not change by a large factor in different wavelengths. Once the supernova fades away, the value of Y_* in various filters can then be determined – a quantity which is slightly harder to measure for lensed quasars, as they are always present and require deblending and simultaneous modeling with the lens galaxy light. Conversely, simultaneous modeling of the supernova half-light radii in various filters with the effects of microlensing may help provide additional constraints on theoretical supernova explosion models (Goldstein et al. 2018; Huber et al. 2019, 2021; Bayer et al. 2021).

We assumed a constant mass-to-light ratio in our simulations, but there is increasing evidence for radial gradients in Y_* from spectroscopy (van Dokkum et al. 2017) and lensing and dynamics (Oldham & Auger 2018; Collett et al. 2018; Sonnenfeld et al. 2018). It should be possible to extend our approach to probe mass-to-light gradients in lens galaxies given the different radii at which lensed macroimages form, though such measurements may be more difficult due to the demagnification of the saddlepoint counterimages – which also have an increased likelihood of yet further microlensing demagnification (Schechter & Wambsganss 2002).

In the next decade gISNe will open a new window onto the population of stars and compact objects in galaxies. With modest investment in follow-up of the LSST gISNe Ia population we should be able to discriminate between a Chabrier and Salpeter IMF with $\sim 4\sigma$ confidence, completely independent of other methods and without the need to assume the dark matter profile of the lens galaxy.

ACKNOWLEDGEMENTS

We would like to thank Scott Gaudi and Enrique Gaztanaga for raising the question of what one can learn about the lens galaxy and microlensing from gISNe Ia if cosmology is known. We thank Paul Schechter for his careful reading and comments.

Numerical computations were done on the Sciama High Performance Compute (HPC) cluster which is supported by the ICG, SEP-Net, and the University of Portsmouth.

This work has received funding from the European Research Council (ERC) under the European Union’s Horizon 2020 research and innovation programme (LensEra: grant agreement No. 945536). TC is funded by the Royal Society through a University Research Fellowship. For the purpose of open access, the authors have applied a Creative Commons Attribution (CC BY) license to any Author Accepted Manuscript version arising.

DATA AVAILABILITY

The simulated data from this work will be made available upon reasonable request to the corresponding author.

REFERENCES

Arendse N., et al., 2024, *MNRAS*, **531**, 3509
 Arendse N., et al., 2025, *arXiv e-prints*, p. [arXiv:2501.01578](https://arxiv.org/abs/2501.01578)
 Auger M. W., Treu T., Bolton A. S., Gavazzi R., Koopmans L. V. E., Marshall P. J., Moustakas L. A., Bures S., 2010, *ApJ*, **724**, 511
 Barnabè M., Spiniello C., Koopmans L. V. E., Trager S. C., Czoske O., Treu T., 2013, *MNRAS*, **436**, 253
 Bayer J., Huber S., Vogl C., Suyu S. H., Taubenberger S., Sluse D., Chan J. H. H., Kerzendorf W. E., 2021, *A&A*, **653**, A29

Bernardi M., et al., 2018, *MNRAS*, **475**, 757
 Cappellari M., 2016, *ARA&A*, **54**, 597
 Cappellari M., et al., 2012, *Nature*, **484**, 485
 Chang K., Refsdal S., 1979, *Nature*, **282**, 561
 Collett T. E., et al., 2018, *Science*, **360**, 1342
 Conroy C., 2013, *ARA&A*, **51**, 393
 Conroy C., Gunn J. E., White M., 2009, *ApJ*, **699**, 486
 Conroy C., van Dokkum P. G., Villaume A., 2017, *ApJ*, **837**, 166
 Dessart L., Hillier D. J., 2005, *A&A*, **439**, 671
 Diego J. M., Bernstein G., Chen W., Goobar A., Johansson J. P., Kelly P. L., Mörtzell E., Nightingale J. W., 2022, *A&A*, **662**, A34
 Dobler G., Keeton C. R., 2006, *ApJ*, **653**, 1391
 Eastman R. G., Schmidt B. P., Kirshner R., 1996, *ApJ*, **466**, 911
 Fabbri R., Costa L. D. F., Torelli J. C., Bruno O. M., 2008, *ACM Comput. Surv.*, **40**
 Falco E. E., Gorenstein M. V., Shapiro I. I., 1985, *ApJ*, **289**, L1
 Foxley-Marrable M., Collett T. E., Vernardos G., Goldstein D. A., Bacon D., 2018, *MNRAS*, **478**, 5081
 Foxley-Marrable M., Collett T. E., Frohmaier C., Goldstein D. A., Kasen D., Swann E., Bacon D., 2020, *MNRAS*, **495**, 4622
 Goldstein D. A., Nugent P. E., Kasen D. N., Collett T. E., 2018, *ApJ*, **855**, 22
 Goldstein D. A., Nugent P. E., Goobar A., 2019, *ApJS*, **243**, 6
 Goobar A., et al., 2017, *Science*, **356**, 291
 Goobar A., et al., 2023, *Nature Astronomy*, **7**, 1098
 Granot J., Schechter P. L., Wambsganss J., 2003, *ApJ*, **583**, 575
 Greengard L., Rokhlin V., 1987, *Journal of Computational Physics*, **73**, 325
 Hsiao E. Y., Conley A., Howell D. A., Sullivan M., Pritchett C. J., Carlberg R. G., Nugent P. E., Phillips M. M., 2007, *ApJ*, **663**, 1187
 Huber S., et al., 2019, *A&A*, **631**, A161
 Huber S., Suyu S. H., Noebauer U. M., Chan J. H. H., Kromer M., Sim S. A., Sluse D., Taubenberger S., 2021, *A&A*, **646**, A110
 Hyde J. B., Bernardi M., 2009, *MNRAS*, **394**, 1978
 Irwin M. J., Webster R. L., Hewett P. C., Corrigan R. T., Jedrzejewski R. I., 1989, *AJ*, **98**, 1989
 Jiménez-Vicente J., Mediavilla E., 2019, *ApJ*, **885**, 75
 Jiménez-Vicente J., Mediavilla E., 2022, *ApJ*, **941**, 80
 Kenworthy W. D., et al., 2021, *ApJ*, **923**, 265
 Kirshner R. P., Kwan J., 1974, *ApJ*, **193**, 27
 Lewis G. F., Gil-Merino R., 2006, *ApJ*, **645**, 835
 Lewis G. F., Irwin M. J., 1995, *MNRAS*, **276**, 103
 Lewis G. F., Irwin M. J., 1996, *MNRAS*, **283**, 225
 Mediavilla E., Muñoz J. A., Lopez P., Mediavilla T., Abajas C., Gonzalez-Morcillo C., Gil-Merino R., 2006, *ApJ*, **653**, 942
 Mediavilla E., et al., 2009, *ApJ*, **706**, 1451
 Mediavilla E., Mediavilla T., Muñoz J. A., Ariza O., Lopez P., Gonzalez-Morcillo C., Jimenez-Vicente J., 2011, *ApJ*, **741**, 42
 Mediavilla E., Jiménez-Vicente J., Muñoz J. A., Vives-Arias H., Calderón-Infante J., 2017, *ApJ*, **836**, L18
 Mortonson M. J., Schechter P. L., Wambsganss J., 2005, *ApJ*, **628**, 594
 Mörtzell E., Johansson J., Dhawan S., Goobar A., Amanullah R., Goldstein D. A., 2020, *MNRAS*, **496**, 3270
 Newman A. B., Smith R. J., Conroy C., Villaume A., van Dokkum P., 2017, *ApJ*, **845**, 157
 Oldham L. J., Auger M. W., 2018, *MNRAS*, **476**, 133
 Paczynski B., 1986, *ApJ*, **301**, 503
 Parravano A., McKee C. F., Hollenbach D. J., 2011, *ApJ*, **726**, 27
 Phillips M. M., 1993, *ApJ*, **413**, L105
 Pielert J. D. R., Rodney S., 2019, *ApJ*, **876**, 107
 Pooley D., Blackburne J. A., Rappaport S., Schechter P. L., Fong W.-f., 2006, *ApJ*, **648**, 67
 Pooley D., Blackburne J. A., Rappaport S., Schechter P. L., 2007, *ApJ*, **661**, 19
 Pooley D., Rappaport S., Blackburne J., Schechter P. L., Schwab J., Wambsganss J., 2009, *ApJ*, **697**, 1892
 Sainz de Murieta A., Collett T. E., Magee M. R., Weisenbach L., Krawczyk C. M., Enzi W., 2023, *MNRAS*, **526**, 4296
 Sainz de Murieta A., Collett T. E., Magee M. R., Pielert J. D. R., Enzi W. J. R., Lokken M., Gagliano A., Ryczanowski D., 2024, *MNRAS*, **535**, 2523

- Schechter P. L., 2018, in Jensen J., Rich R. M., de Grijs R., eds, *Astronomical Society of the Pacific Conference Series Vol. 514, Stellar Populations and the Distance Scale*. p. 79 ([arXiv:1712.00393](https://arxiv.org/abs/1712.00393)), [doi:10.48550/arXiv.1712.00393](https://doi.org/10.48550/arXiv.1712.00393)
- Schechter P. L., Wambsganss J., 2002, *ApJ*, **580**, 685
- Schechter P. L., Wambsganss J., Lewis G. F., 2004, *ApJ*, **613**, 77
- Schechter P. L., Pooley D., Blackburne J. A., Wambsganss J., 2014, *ApJ*, **793**, 96
- Schmidt R. W., Wambsganss J., 2010, *General Relativity and Gravitation*, **42**, 2127
- Schneider P., Sluse D., 2014, *A&A*, **564**, A103
- Shajib A. J., Treu T., Birrer S., Sonnenfeld A., 2021, *MNRAS*, **503**, 2380
- Shajib A. J., et al., 2024, *Space Sci. Rev.*, **220**, 87
- Smith R. J., 2020, *ARA&A*, **58**, 577
- Sonnenfeld A., Treu T., Gavazzi R., Marshall P. J., Auger M. W., Suyu S. H., Koopmans L. V. E., Bolton A. S., 2012, *ApJ*, **752**, 163
- Sonnenfeld A., Treu T., Marshall P. J., Suyu S. H., Gavazzi R., Auger M. W., Nipoti C., 2015, *ApJ*, **800**, 94
- Sonnenfeld A., Leauthaud A., Auger M. W., Gavazzi R., Treu T., More S., Komiyama Y., 2018, *MNRAS*, **481**, 164
- Sonnenfeld A., Jaelani A. T., Chan J., More A., Suyu S. H., Wong K. C., Oguri M., Lee C.-H., 2019, *A&A*, **630**, A71
- Spiniello C., Koopmans L. V. E., Trager S. C., Czoske O., Treu T., 2011, *MNRAS*, **417**, 3000
- Spiniello C., Trager S. C., Koopmans L. V. E., Chen Y. P., 2012, *ApJ*, **753**, L32
- Suyu S. H., Goobar A., Collett T., More A., Vernardos G., 2024, *Space Sci. Rev.*, **220**, 13
- Takáts K., Vinkó J., 2012, *MNRAS*, **419**, 2783
- Treu T., Koopmans L. V. E., 2004, *ApJ*, **611**, 739
- Treu T., Auger M. W., Koopmans L. V. E., Gavazzi R., Marshall P. J., Bolton A. S., 2010, *ApJ*, **709**, 1195
- Vernardos G., 2019, *MNRAS*, **483**, 5583
- Vernardos G., Fluke C. J., 2014, *MNRAS*, **445**, 1223
- Vernardos G., Tsagkatakis G., 2019, *MNRAS*, **486**, 1944
- Vernardos G., et al., 2024, *Space Sci. Rev.*, **220**, 14
- Walsh D., Carswell R. F., Weymann R. J., 1979, *Nature*, **279**, 381
- Wambsganss J., 1992, *ApJ*, **386**, 19
- Wambsganss J., Witt H. J., Schneider P., 1992, *A&A*, **258**, 591
- Weisenbach L., Schechter P. L., Pontula S., 2021, *ApJ*, **922**, 70
- Weisenbach L., Collett T., de Murieta A. S., Krawczyk C., Vernardos G., Enzi W., Lundgren A., 2024, *MNRAS*, **531**, 4349
- Witt H. J., 1990, *A&A*, **236**, 311
- Witt H. J., Mao S., Schechter P. L., 1995, *ApJ*, **443**, 18
- Wojtak R., Hjorth J., Gall C., 2019, *MNRAS*, **487**, 3342
- Wyithe J. S. B., Turner E. L., 2001, *MNRAS*, **320**, 21
- Young P., 1981, *ApJ*, **244**, 756
- Zheng W., Kelly P. L., Filippenko A. V., 2018, *ApJ*, **858**, 104
- van Dokkum P., Conroy C., 2024, *ApJ*, **973**, L32
- van Dokkum P., Conroy C., Villaume A., Brodie J., Romanowsky A. J., 2017, *ApJ*, **841**, 68

APPENDIX A: JOINT CONSTRAINTS ON α_{IMF} AND m_{\star}

In Figure A1, we show joint constraints on α_{IMF} and m_{\star} for either 50 or 200 gISNe Ia systems, with errors on the intrinsic source brightness varying from 0.1 to 0.3 mag. The true values $\alpha_{\text{IMF}} = 1$ and $m_{\star} = 0.3M_{\odot}$ lie within or near the 68% confidence intervals for the joint posteriors, though α_{IMF} lies slightly outside the 68% interval of its marginalized posterior when the error on the source brightness is large. This is likely due to the multimodal nature of the microlensing likelihoods playing a larger role when the prior on the source brightness is wider.

This paper has been typeset from a $\text{\TeX}/\text{\LaTeX}$ file prepared by the author.

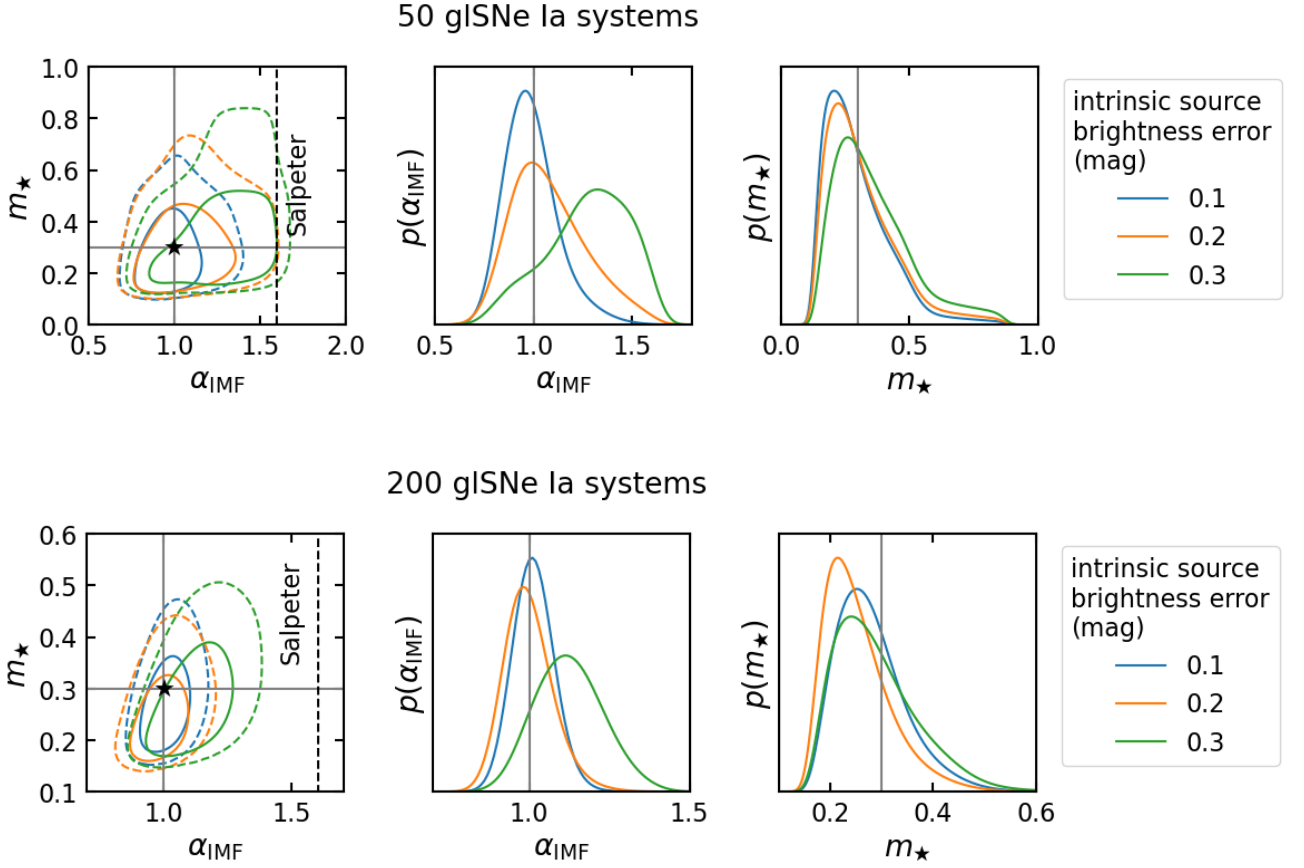


Figure A1. Joint posterior of α_{IMF} and m_{\star} for 50 or 200 gISNe Ia systems, assuming various errors on the intrinsic source brightness, a uniform prior on α_{IMF} such that $\kappa_{\star} \leq \kappa$, and a uniform prior between 0 and $1 M_{\odot}$ for m_{\star} . Solid and dashed contours denote the 68% and 95% confidence intervals respectively, while the black dashed line marks the approximate value of α_{IMF} for a Salpeter IMF. Note the different axes ranges between the top and bottom plots.